Advanced Meta-Modeling framework combining Machine Learning and Model Order Reduction towards real-time virtual testing of woven composite laminates in nonlinear regime

M. El Fallaki Idrissi [a,b,*], A. Pasquale [b], F. Meraghni [a], F. Praud [a], F. Chinesta [b]

[a] Arts et Métiers Institute of Technology, CNRS, LEM3-UMR 7239, 4 rue Augustin Fresnel, 57078 Metz, France
[b] ESI Chair, Arts et Métiers Institute of Technology, CNRS, PIMM-UMR 8006, 151 Boulevard de l'Hôpital, 75013 Paris, France

A B S T R A C T

This paper presents an advanced meta-modeling framework that efficiently combines Machine Learning and Model Order Reduction (MOR) techniques for real-time virtual testing of woven composite materials. The framework is specifically designed to develop a multiparametric solution capable of accurately predicting the macroscopic nonlinear stress–strain curves of woven composite laminates submitted to loading–unloading paths. It takes into account five key microstructural parameters: yarn weft width, yarn warp width, yarn spacing, fabric thickness as well as the reinforcement orientation. The methodology employs the Proper Orthogonal Decomposition (POD) technique to decompose the stress–strain curves, extracting principal features that effectively characterize the overall composite's response. Subsequently, a Random Forest machine learning model is applied to interpolate these features across the microstructural parameter space, allowing for rapid retrieval of corresponding features for any new laminate configuration in the nonlinear regime. A key advantages of this approach is its capacity to dynamically generate extensive virtual test databases, in real-time, across a wide range of composite laminate configurations. This capability provides a comprehensive and efficient tool for analyzing and optimizing composite performance while substantially reducing both experimental and computational costs. Furthermore, to enhance usability for engineers and researchers, this multiparametric solution has been integrated into a user-friendly Graphical User Interface (GUI) application. This GUI empowers users to easily explore various laminate configurations, visualize results, and conduct virtual testing, establishing the framework as a powerful tool for real-time virtual testing and in-depth analysis of microstructural effects on composite materials.

1. Introduction

Composite has become an indispensable material in structural applications where light-weight and high-strength is expected, like it is often the case in aeronautics, automotive and other transportation industries [1]. This demand has increased with the growing sustainable trends of electric and hydrogen vehicles, which aim at reducing the environmental impact induced by CO_2 emissions [2]. Beside this, various innovative solutions, and new recycling technologies (thermal, chemical, and mechanical recycling) have been developed to give these materials a new life once they have been discarded [3–5]. These advancements not only enhance the value of recycled composites but also reduce the cost of extracting new raw materials and minimize the environmental burden associated with material waste, whether through incineration or environmental dispersion. Moreover, advances in composites manufacturing and process design have led to the emergence of several types of composite offering distinct characteristics depending on industry needs, such as fiber- and woven-reinforced composites with thermoplastic or thermoset polymer matrix, etc [6,7].

Despite their numerous advantages, the widespread application of composite materials has been impeded by the complexities involved in understanding and predicting their overall mechanical behavior. To address these challenges, extensive scientific research has been conducted utilizing both numerical and experimental methods. Multiscale approaches have proven particularly effective in analyzing the microstructural heterogeneities of composites, enabling researchers to understand the mechanisms and phenomena that occur across different scales, from micro- to macro-scale [8]. Basically, two approaches can be distinguished. Those based on Eshelby's equivalent inclusion theory, known as mean-field approaches, such as the Mori–Tanaka scheme,

* Corresponding author at: Arts et Métiers Institute of Technology, CNRS, LEM3-UMR 7239, 4 rue Augustin Fresnel, 57078 Metz, France.
E-mail address: mohammed.el_fallaki_idrissi@ensam.eu (M. El Fallaki Idrissi).

self-consistent or other extended computational approaches [9–12]. Other so-called full-field approaches, where homogenization is performed using Finite Volumes, Boundary Elements, Finite Elements or Fast Fourier Transform, etc [13–18]. The latter generally provide more robust macroscopic stress–strain predictions for composites than mean-field approaches. Indeed, using it often requires huge computing resources, which hampers real-time decision-making and heightens the complexity of the design and optimization processes.

Moreover, the computational challenges in understanding composite materials are significantly amplified by the multitude of factors involved, including microstructural morphology, material properties, manufacturing processes, and service conditions. In this context, extensive research has shown that environmental factors, including temperature fluctuations, water uptake and chemical aging, can have an impact on the mechanical and physical properties of composites [19–22]. Similarly, other studies have emphasized the influence of parameters like pressure, layer thickness, and strong hydrogen interactions on the performance and safety of composite tanks [23,24]. Furthermore, several studies have illustrated how microstructural architecture and the characteristics of composite constituents affect the macroscopic response of these materials [25,26]. A comprehensive understanding of the factors influencing composite materials is essential for advancing their applications across various industries. While multiscale modeling using the finite element method is a valuable tool for this purpose, it presents significant challenges due to its high computational cost. This challenge becomes even more pronounced in scenarios where simulations need to be repeated for varying parameter values, leading in a significant increase in computational cost. Additionally, the composites industry increasingly demands rapid and accurate predictions of composite structure's responses for effective real-time monitoring and decision-making. To meet this critical need, various Model Order Reduction (MOR) techniques and Machine Learning algorithms (ML) [27,28] have been developed to create meta-models and multiparametric solutions. These innovative approaches enable, *on-the-fly*, predictions of composite behavior as parameters are adjusted.

The Proper Generalized Decomposition (PGD) method and particularly its non-intrusive variant, has been successfully employed across various scientific and engineering domains as a MOR technique. By separating variables such as space, time, loading conditions, material properties, or morphologic parameters, PGD creates computational vademecums and virtual charts that enable the optimization and real-time simulation of complex problems [27,29]. This approach facilitates the industry's transition to digital, virtual and hybrid twin paradigms [30]. PGD has proven effective in a variety of parameterized applications, including composite materials [31,32], welding processes [33], vehicle crash analysis [34], or electromagnetic field simulations [35,36]. Meanwhile, Machine learning (ML) and deep learning (DL) techniques have become powerful tools for analyzing, modeling, optimizing, and monitoring composite structures [37–39]. These methods demonstrate great potential in addressing the complexities of multiscale and multiparametric modeling [40]. In fact, ML has significantly reduced the computational costs associated with multiscale simulations, such as FE^2 by developing Artificial Neural Network (ANN)-based surrogate models. These models effectively replace traditional finite element (FE) calculations at the microscopic scale, offering more efficient multiscale simulations [41–45]. This is further advanced by the development of physics-based machine learning models, that ensure adherence to fundamental physical and thermodynamic laws, thereby improving the models' predictive capabilities [46,47]. On the other hand, ML-based models have also proven valuable in developing multiparametric solutions for composites, taking into account a wide range of factors, including material composition, manufacturing parameters, and environmental conditions [48–50].

Recently, a multiparametric solution was developed in [32], employing non-intrusive PGD methods to evaluate the macroscopic elastic properties of woven reinforcement composites in a quasi-instantaneous manner. This solution takes into account various microstructural parameters, including weave architecture, microstructural morphology, and matrix/fiber material properties. In related research work [51], non-intrusive PGD was applied to interpolate the strain–stress curves for viscoelastic–viscoplastic behavior of composites at a fixed woven laminate orientation. In this work, we extend the parametric solution to predict the nonlinear stress–strain behavior of woven composites by incorporating microstructural parameters and fabric orientation into a framework that integrates machine learning and MOR techniques. The methodology employs Proper Orthogonal Decomposition (POD) to decompose the stress–strain curves, extracting principal features that effectively characterize the material's response. A machine learning algorithm is then implemented to interpolate these features across the microstructural parameter space, providing a more efficient alternative to direct curve interpolation. To this end, virtual tests were precomputed for various microstructures and laminate configurations during an *offline* stage, using a nonlinear multiscale model that incorporates anisotropic damage in the yarns and an elasto-plastic behavior for the matrix, as detailed in [52–54]. This approach facilitates a fast examination of how microstructure and the woven fabric orientation affect the macroscopic nonlinear behavior of composites, simplifying the optimization process for composite structures. Additionally, the framework significantly reduces costs by minimizing the reliance on experimental testing and traditional numerical simulations when variations in the composite microstructure occur. The solution developed in this work is tested and validated on a laminated composite with a polyamide 66 matrix and a 2/2 twill weave reinforcement architecture.

The remainder of the paper is organized as follows: In Section 2, we introduce the parametric representation of the problem, which includes the microstructure morphology, the woven fabric orientation, and the loading conditions. In Section 3, we provide an overview of the nonlinear multiscale modeling approach, as well as local constitutive models that are utilized for both yarns and matrix materials, with more detailed descriptions available in Appendix. This section also presents the results of virtual testing, featuring stress–strain curves for four distinct laminate configurations and a comparative analysis with experimental data. Section 4 outlines the framework that integrates Model Order Reduction (MOR) and Machine Learning techniques. Finally, the last section discusses the results, demonstrating the accuracy and robustness of the proposed methodology. Additionally, a GUI application designed to facilitate the visualization of the parametric solution is presented, along with concluding remarks.

2. Parametric non-linear homogenized response for woven composites

Although FE-based multiscale models can be utilized in conjunction with the FE^2 method [55–57] for structural analyses, such a numerical process remains, in practice, poorly attractive in the context of industrial applications, due to the considerable computational resources it requires. Alternatively, one can consider multiscale models to generate in the first place a batch of virtual tests, that can be employed afterwards to identify macro-phenomenological models [58–61]. Those are much less computationally demanding, but in return, may require a certain amount of experimental data for their identification. Besides being costly to obtain, these experimental data are only valid for one single microstructure configuration. Therefore, using a multiscale model to perform these virtual tests becomes a sound compromise. Of course, this can be done for any set of microstructural parameters. However, depending on the number of considered parameters as well as the number of necessary virtual tests to perform, this still requires a certain computational resource which remains practically inconvenient in industrial applications. In this context, an approximated solution containing all the particular solutions for any set of microstructural parameters would be a valuable asset towards real-time virtual test predictions. It will also provides a comprehensive understanding of

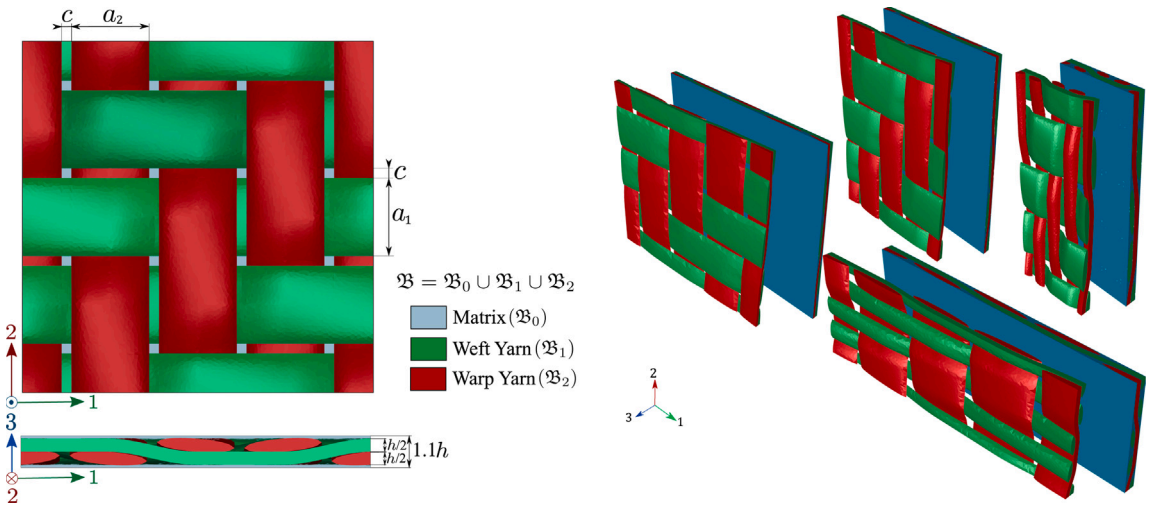

(a) Parametric representation of the microstructure for 2-2 twill weave composites.

(b) Examples of generated unit-cell meshes for various set of microtructural parameters.

Fig. 1. Parametric representation of woven composite microstructure (Unit-cell) and examples of resulting microstructures due to geometric changes. (a) The unit cell geometry parameters: the weft yarn width a_1, the warp yarn width a_2, the fabric thickness h and the gap between two adjacent yarns c. (b) Examples of automatically generated unit-cell meshes, illustrating yarn configurations and complete unit cells for different sets of microstructural parameters. The unit cell on the left represents the reference parameter set (*cf.*, Table 1).

the microstructure impact on composite response, making it easier to optimize composite structures and achieve the desired mechanical performance. These possibilities arise from the online evaluation of the macroscopic response, almost in real-time, for any set of parameters. In the case of woven composite materials, the architecture of the reinforcement specifically, the fabric geometry and the properties of its constituent phases, plays a crucial role in determining macroscopic behavior. To this end, the present study develops a multiparametric solution to capture and account for the effects of these parameters.

2.1. Parametric representation of the solution

This work focuses on the analysis of symmetrical and balanced laminated composites reinforced with a 2/2 twill weave architecture embedded into a polymer matrix. The characteristics and properties of the composite are described using a Unit Cell (UC), as illustrated in Fig. 1(a). The unit cell domain, denoted as $\mathfrak{B}$, consists of three distinct phases: the matrix phase, labeled as $\mathfrak{B}_0$, and the weft and warp yarn phases, represented by the subdomains $\mathfrak{B}_1$ and $\mathfrak{B}_2$, respectively. Fig. 1(a), illustrates the geometry of the 2/2 twill microstructure, modeled by assuming an elliptical shape for the yarns. This geometry can be characterized using four independent parameters: the weft yarn width a_1, warp yarn width a_2, fabric thickness h, and the gap c between yarns. Both the weft and warp yarns share the same thickness, which is equal to half the total fabric thickness h, and the gap c is assumed to be uniform for both sets of yarns.

As illustrated in Fig. 2, the symmetrical and balanced laminated composite $[\pm\theta]_s$ is oriented at an angle θ with respect to the loading axis $\vec{x}$. This angle θ serves as the fifth parameter of the problem, alongside the four geometrical parameters mentioned above. Together, these parameters define a 5-dimensional parameter space, represented by the vector $\boldsymbol{p} = \{p_1\ p_2\ p_3\ p_4\ p_5\}^T$ containing all the previously mentioned quantities. The components of $\boldsymbol{p}$ are listed in Table 1, along with their respective value ranges. These ranges cover a wide spectrum of laminated composite configurations that can be found in industry. Furthermore, a reference set of parameters for which experimental data is available from previous studies [54,62] is also provided in Table 1.

The meta-modeling framework developed in this study is designed to predict the macroscopic strain resulting from an applied macroscopic stress during a uniaxial load–unload test, while varying the characteristics of composite laminate. The schematic representation of this simulation is illustrated in Fig. 3, where the material is subjected to a cyclic triangular stress signal (Load–Unload test) under progressively increasing amplitudes corresponding to 25%, 50%, 75%, and 100% of the maximum stress $\overline{\sigma}_{\max}$. The maximum stress depends on the woven fabric orientation in the laminate (θ). For example, when $\theta = 0°$, the maximum stress $\overline{\sigma}_{\max}$ is 400 MPa, whereas for $\theta = 45°$, $\overline{\sigma}_{\max}$ drops to 100 MPa. This is visually depicted in Fig. 3(a), providing a 3D representation of the applied stress–time curve as a function of the angle θ. Alternatively, Fig. 3(b) offers a 2D representation showing the applied macroscopic stress–time for specific examples of laminates for instance $[\pm 0°]_s$ and $[\pm 45°]_s$.

To effectively train and evaluate the developed framework, a dataset comprising 870 samples is generated, which is then split into two parts: 80% for training and 20% for testing. Each input vector in the dataset, denoted as ($\boldsymbol{p}$) is associated with an output vector ($\boldsymbol{s}$) that represents the macroscopic strain–time curve. The dataset generation process begins with the automatic creation and meshing of unit cell, guided by predefined parameters and their respective ranges. Examples of unit cells are illustrated in Fig. 1(b) that includes the reference microstructure used for the experimental results. This meshing process is performed through Python scripts developed specifically within the *TexGen* framework [63,64]. The resulting mesh consisted of first-order tetrahedral elements (C3D4), chosen for their balance of accuracy and computational efficiency. Although the meshing process was largely automated, particular attention was required for unit cells with complex geometries. Specifically, challenges were encountered in regions where the gap between adjacent yarns was very small. To address this, additional care was taken to refine the mesh in these areas, ensuring high mesh quality and avoiding irregularities that could induce singularities. Each simulation was performed using the Arts et Métiers High-Performance Computing Center, *Cassiopee*. The CPU time for individual simulations ranged from 2500 to 3500 seconds. The total CPU time required for all simulations used for training and testing amounted to approximately 25.10^5 seconds. However, as many simulations were executed in parallel, the computational time required for dataset generation was significantly reduced. Following the generation of unit cells, local constitutive models are assigned to each phase and

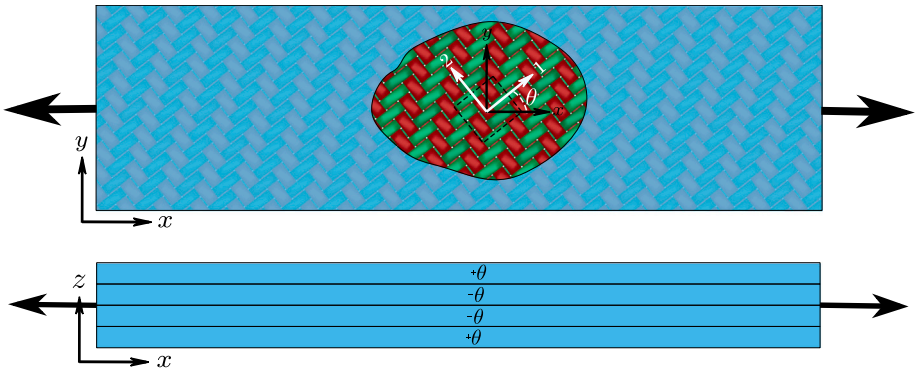

Fig. 2. Symmetric and balanced laminate composite $[\pm\theta]_s$ subjected to axial loading test.

Table 1
Microstructural parameters for 2-2 twill weave composites. Each one of them ranging from a minimum value to a maximum value. These ranges defines a 5-dimensional parametric space that covers a wide spectrum of possible laminates with 2-2 twill weave microstructures. A reference set of parameters for which experimental data are available from previous works [54,62] is also provided.

Parameter	Description	Ref. value	Min. value	Max. value	Unit
p_1	Weft yarns width a_1	3.46	0.8	4.5	mm
p_2	Warp yarns width a_2	3.46	0.8	4.5	mm
p_3	Fabric thickness h	0.45	0.2	0.6	mm
p_4	Gap between two adjacent yarns c	0.29	0.3	0.6	mm
p_5	Orientation θ	0/15/30/45	0	90	deg [°]

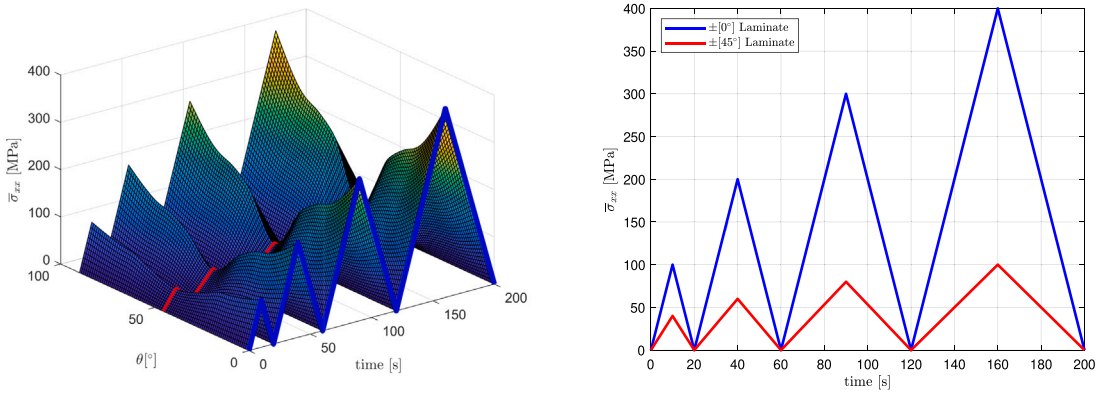

(a) Macroscopic stress-time loading path applied to the laminate, as a function of the woven fabric orientation θ.

(b) Stress-time loading path applied to the $[\pm 0°]_s$ and $[\pm 45°]_s$ laminates.

Fig. 3. Applied macroscopic stress $\overline{\sigma}_{xx}(\theta, t)$ on a $[\pm\theta°]_s$ laminate during loading–unloading test.

a nonlinear periodic homogenization approach is applied to accurately capture the macroscopic strain for an applied macroscopic stress.

3. Multiscale modeling approach and local constitutive laws

3.1. Non-linear periodic homogenization

Periodic homogenization, as a multiscale modeling approach, establishes a bridge between the microscopic and macroscopic scales of materials that account for the separation of scales [65–67]. This connection is typically defined by averaging the microscopic stress and strain over the entire unit cell domain $\mathfrak{B}$ as follows:

$$\overline{\boldsymbol{\sigma}}(t) = \frac{1}{V}\int_{\mathfrak{B}} \boldsymbol{\sigma}(\boldsymbol{x}, t)\, \mathrm{d}V, \tag{1a}$$

and

$$\overline{\boldsymbol{\varepsilon}}(t) = \frac{1}{V}\int_{\mathfrak{B}} \boldsymbol{\varepsilon}(\boldsymbol{x}, t)\, \mathrm{d}V, \tag{1b}$$

where V denotes the volume of the unit-cell.

In this multiscale approach, considering the periodicity of the UC, periodic boundary conditions are imposed [68,69]. As a result, the displacement field $\boldsymbol{u}$ within the unit cell can be expressed in Eq. (2). This equation comprises an affine part $\overline{\boldsymbol{\varepsilon}} \cdot \boldsymbol{x}$, a periodic fluctuation $\tilde{\boldsymbol{u}}$ and an eventual rigid body motion $\boldsymbol{u}_0$:

$$\boldsymbol{u}(\boldsymbol{x}, t) = \overline{\boldsymbol{\varepsilon}}(t) \cdot \boldsymbol{x} + \tilde{\boldsymbol{u}}(\boldsymbol{x}, t) + \boldsymbol{u}_0(t), \qquad \forall \boldsymbol{x} \in \mathfrak{B}. \tag{2}$$

where $\tilde{\boldsymbol{u}}$ takes same values ($\tilde{\boldsymbol{u}}(\boldsymbol{x}_+, t) = \tilde{\boldsymbol{u}}(\boldsymbol{x}_-, t)$) at each pair of opposite points $\boldsymbol{x}_+$ and $\boldsymbol{x}_-$ lying on the unit cell borders $\partial\mathfrak{B}$. Based on the aforementioned equations, the Periodic Boundary Conditions (PBCs)

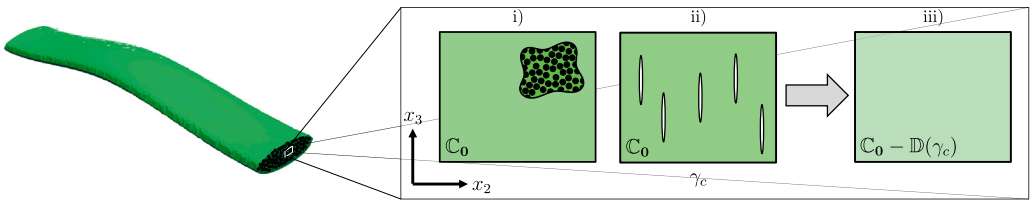

Fig. 4. Schematic representation of yarn damage law.

can be defined as follows:

$$\boldsymbol{u}(\boldsymbol{x}_+, t) - \boldsymbol{u}(\boldsymbol{x}_-, t) = \overline{\boldsymbol{\varepsilon}}(t) \cdot (\boldsymbol{x}_+ - \boldsymbol{x}_-), \qquad \forall \boldsymbol{x}_+, \boldsymbol{x}_- \in \partial\mathfrak{B}. \tag{3}$$

To solve the macroscopic stress–strain response for a given loading path, in this case, for a macroscopic stress loading path, the local equilibrium equations, along with periodic boundary conditions (PBCs) and scale transition relationships, are applied. This is typically achieved through finite element simulations using a formalism that associates the dual forces with the constraint drivers as proposed in [62,70–72].

3.2. Local constitutive models

In this study, two constitutive models are employed to characterize the behavior of both the yarns and the matrix material. This section provides a brief overview of these models, while further details, including the constitutive equations, are available in Appendix. The matrix phase consists of PA66 polymer, which is known for its distinctive yielding characteristics, encompassing both viscoelastic and viscoplastic behavior. In this work, the matrix behavior is idealized and modeled using a classical elastoplastic constitutive framework that includes isotropic hardening, as outlined by [73–75]. The material parameters for the matrix, were identified using established elastoplastic modeling techniques [74] and experimental data from monotonic tests reported in previous research [53,62]. These parameters are summarized in Table A.3. Fig. 5(a) illustrates a strong agreement between the experimental monotonic response of the PA66 matrix and the model predictions under a strain of 8%. It is important to note that the experimental test was conducted at a low strain rate of $\dot{\varepsilon} = 8.10^{-4}$ s^{-1} to mitigate viscous and rate-dependent effects (viscoelastic and viscoplastic), ensuring a focus on the material's elastoplastic behavior. The yarns, in contrast, consist of continuous reinforcement, *i.e.*, long fibers, embedded in the matrix. At the scale of interest, such a composite typically exhibits a linear elastic response up to brittle failure in the longitudinal direction. However, the transverse response and/or in-plane shear, display progressive damage and inelastic behavior due to the diffuse growth of micro-cracks. These cracks originate at the fiber/matrix interfaces through debonding and propagate through coalescence. The behavior of the yarns is modeled using a hybrid micromechanical-phenomenological constitutive framework, as developed in [52,62], and schematically illustrated in Fig. 4, with the main constitutive equations provided in Appendix A.2.

Unlike the matrix, mechanical testing on the yarns cannot be performed directly, as they cannot be isolated from the woven composite. Therefore, the parameters for the yarns are identified indirectly through reverse engineering techniques, based on the macroscopic response of the entire woven composite, as outlined by [76,77] for the reference microstructure (see Table 1). Figs. 5(b)–5(d) show the associated longitudinal, transverse and in-plane shear predicted responses of the yarns, respectively. The identified parameters for the yarn model are summarized in Table A.4.

3.3. Virtual testing on $[\pm\theta]_s$ laminates

Woven composites are generally characterized from tensile tests on $[\pm\theta]_s$ laminates, as depicted in Fig. 2. Such a symmetric and balanced laminate configuration conveniently results in vanishing tension/in-plane shear and tension/curvature couplings. Thus, a $[\pm\theta]_s$ laminate loaded with an axial stress $\overline{\sigma}_{xx}$ only responds in terms of axial and transverse strain, $\overline{\varepsilon}_{xx}$ and $\overline{\varepsilon}_{yy}$, respectively. Furthermore, cyclic tests with increasing stress levels are usually performed to highlight the gradual apparent stiffness reduction due to damage as well as the increase in inelastic strain at the scale of the whole composite. Such data are then useful for the identification of macro-phenomenological models of the whole woven composite [58–61] that are more practical in the context of industrial applications.

Figs. 6(a), 6(b), 6(c) and 6(d) show, in the case of the reference microstructural parameters, the comparison between the experimentally recorded laminate response and the one computed with the multiscale model for $[\pm 0°]_s$, $[\pm 15°]_s$, $[\pm 30°]_s$ and $[\pm 45°]_s$ laminates, respectively.

Note that, on the one hand, the responses with the $[\pm 0°]_s$ and $[\pm 45°]_s$ laminates were used for the identification of the yarns parameters, (*cf.*, Table A.4), for which very good agreements were achieved. On the other hand, the responses with the $[\pm 15°]_s$ and $[\pm 30°]_s$ laminates were kept for validation, which is rather satisfying.

One can notice that the response of the $[\pm 0°]_s$ laminate, shown in Fig. 6(a), is nearly linear. Indeed, in this case, most of the macroscopic stress is carried by the weft yarns in their longitudinal direction for which they elastically behave with an important stiffness. Besides the matrix, a minor part of the macroscopic stress is also carried by the warp yarns in their transverse direction, resulting in a rather low micro-cracks occurrence. In the case of the $[\pm 45°]_s$ laminate, the overall response of the composite, shown in Fig. 6(d), exhibits much more degradation and inelastic deformations.

4. Model order reduction and machine learning

Model Order Reduction (MOR) is a branch of computational science focused on reducing the computational cost associated with simulating or analyzing complex models. This achieves by creating simplified versions, or reduced-order models, that accurately capture the system's dynamics. This approach facilitates faster simulations, optimization, and control design without significant loss of fidelity. MOR is particularly advantageous for high-dimensional or parametric systems, commonly encountered in engineering and scientific applications. For an extensive overview of state-of-the-art MOR techniques, the reader is referred to the works of [78–80]. In this context, we revisit a general procedure for constructing parametric surrogate model of macroscopic stress–strain curves.

Let us consider the dataset at hand, which consists of input parameters $\boldsymbol{p} = \{p_k\}_{k=1,\dots,N}$ and their corresponding output curves $s(t;\boldsymbol{p})$, as previously described and illustrated later in Fig. 8. Each curve represents the macroscopic response of the laminated composite with different types of reinforcement, characterized by the parameters $\boldsymbol{p}$. Thus, each data point can be viewed as a snapshot $(\boldsymbol{p}_i, s(t;\boldsymbol{p}_i))$, where $i = 1, 2, \dots, n_s$, representing the specific combination of input parameters and the resulting output curve. Here the solution $s(t;\boldsymbol{p})$ is typically obtained via finite element analysis, however different sources of data may also be incorporated.

Before building a regression model to approximate the curve in the parametric space, dimensionality reduction techniques such as Principal Component Analysis (PCA) or Proper Orthogonal Decomposition

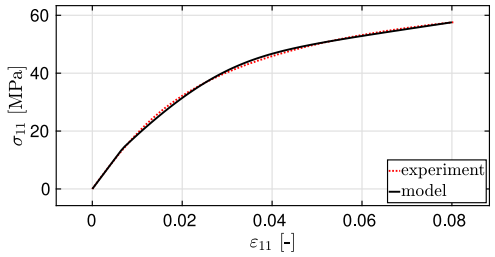

(a) Uni-axial monotonic response of the PA66 matrix.

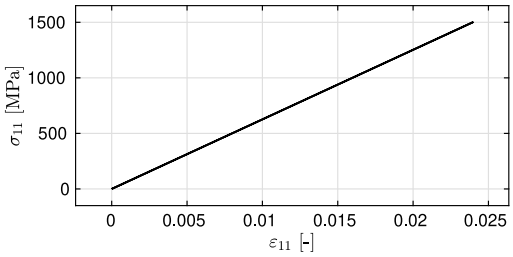

(b) Longitudinal response of the yarns.

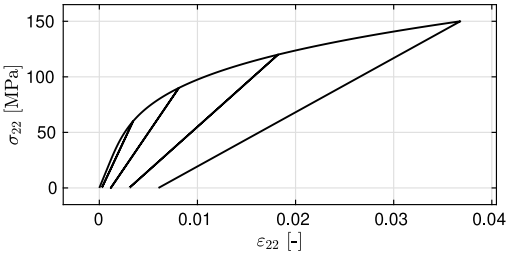

(c) Transeverse reponse of the yarns.

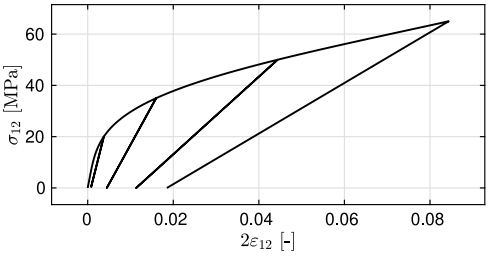

(d) In-plane shear response of the yarns.

Fig. 5. Uni-axial monotonic response of the PA66 matrix. Comparison between the experiment and the elastoplastic model. Computed longitudinal, transverse and in-plane shear responses of the yarns upon loading/unloading cycles with increasing stress levels.

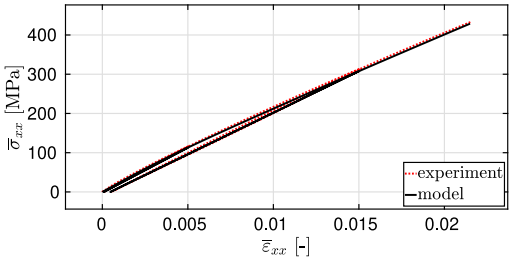

(a) Response of the $[\pm 0^\circ]_s$ laminate.

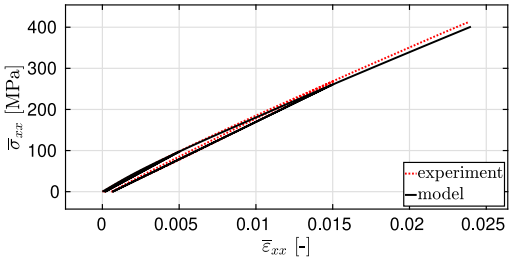

(b) Response of the $[\pm 15^\circ]_s$ laminate.

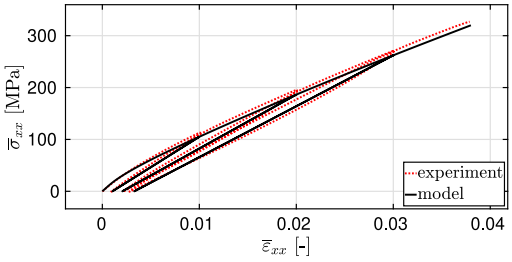

(c) Response of the $[\pm 30^\circ]_s$ laminate.

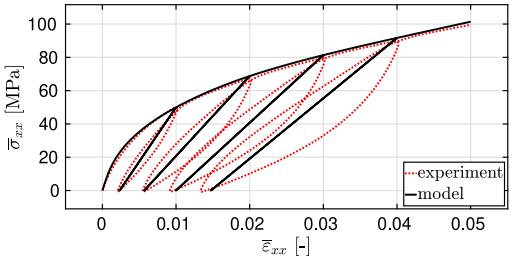

(d) Response of the $[\pm 45^\circ]_s$ laminate.

Fig. 6. Comparison of experimental and finite element-based periodic homogenization results for the macroscopic response of laminate composites that have the same reinforcement (Reference microstructure in Table 1) according to different woven fabric orientations: $[\pm 0^\circ]_s$, $[\pm 15^\circ]_s$, $[\pm 30^\circ]_s$, and $[\pm 45^\circ]_s$.

(POD) are applied directly to the output curves $s(t;\boldsymbol{p}_i)$ to extract the dominant modes of variability. This allows us to represent the curve using a limited number of coefficients and modes, which effectively capture the essential features of the output curves, rather than considering all data points along the curve. To achieve this, reduced basis functions $\phi_j(t)$ are constructed. These functions are utilized to develop a surrogate model $\hat{s}(t,\boldsymbol{p})$, which approximates the output curves $s(t;\boldsymbol{p}_i)$ based on the inputs $\boldsymbol{p}_i$ and the time t. Therefore, we can write the equation as:

$$\hat{s}(t,\boldsymbol{p}) = \sum_{j=1}^{M} \lambda_j(\boldsymbol{p})\phi_j(t), \tag{4}$$

where $\lambda_j(\boldsymbol{p})$ are the coefficients of the surrogate model, which may depend on the inputs $\boldsymbol{p}$.

Instead of approximating all points on the curve $s(t;\boldsymbol{p})$. the surrogate model can now be designed specifically to estimate the coefficients

$\lambda_j(\boldsymbol{p})$. The full curve can then be efficiently reconstructed using the previously defined POD basis functions. To achieve this, the regression algorithm is trained on the dataset to establish a relationship between the input parameters and their corresponding output coefficients. In this context, numerous machine learning algorithms are available in the literature for constructing such regression functions. For example, linear regression is the most basic technique, which assumes a linear relationship between the input and variables. In contrast, polynomial regression extends this concept by considering polynomial relationships. Regularized regression methods are also widely recognized such as Ridge regression or Lasso regression. Ridge regressions, or L^2-regularization, introduces a penalty term in linear regression to prevent overfitting. In contrast, Lasso regression, known for its L^1-regularization, introducing a penalty that can shrink some coefficients to zero, resulting in sparse models. For polynomial regression approaches, further insights can be found in works discussing linear and regularized regression techniques [81]. The literature also presents a variety of other regression techniques. For example, Support Vector Regression (SVR) adapts the concepts of Support Vector Machines (SVMs) to handle regression problems by identifying a hyperplane that optimally represents the data [82]. Additionally, decision trees can be utilized for regression by dividing the data into smaller groups and predicting outcomes based on the average target value within each group [83]. Furthermore, Random Forest regression, which is an ensemble learning approach, improves prediction accuracy and mitigates overfitting by combining the results of multiple decision trees [84]. In the context of polynomial regressions, innovative strategies based on Proper Generalized Decomposition (PGD) can also be employed to tackle the challenges associated with high-dimensional parametric problems [85–87]. In particular, in the context of parametric curves metamodelling many advances have been proposed employing the sPGD gaining a growing interest in different fields of engineering [88], such as automotive crashworthiness and lightweight optimization [89], electric batteries design [90,91], or manufacturing processes [92]. Moreover, manifold-based interpolation techniques, such as those using the Grassmann manifolds, are particularly useful for approximating data in high-dimensional spaces, providing an effective approach to complex parametric modeling [93,94]. Finally, deep learning techniques [95], particularly Artificial Neural Networks (ANNs), can be used for regression tasks by effectively capturing complex relationships between input and output variables.

4.1. POD-based modes extraction

Given the training output curves $\{s_i(t)\}_{i=1}^{n_s}$, for $t \in T = \{t_j\}_{j=1}^{n_t}$, a matrix of snapshots can be constructed as follows:

$$\mathbf{S} = \begin{bmatrix} \boldsymbol{s}_1 & \boldsymbol{s}_2 & \dots & \boldsymbol{s}_{n_s} \end{bmatrix} \in \mathbb{R}^{n_t \times n_s}, \tag{5}$$

where each column vector $\boldsymbol{s}_i \in \mathbb{R}^{n_t \times i}$ contains the values of $s(t)$ sampled at the discrete time points in T.

To reduce the dimensionality of this snapshots matrix, we apply a truncated POD of rank r, yielding the following approximate:

$$\mathbf{S} \approx \mathbf{U}\boldsymbol{\Sigma}\mathbf{V}^{\mathrm{T}} \tag{6}$$

where $\mathbf{U} \in \mathbb{R}^{n_t \times r}$, $\boldsymbol{\Sigma} \in \mathbb{R}^{r \times r}$, $\mathbf{V} \in \mathbb{R}^{n_s \times r}$. From this decomposition, we define the matrices of POD modes and corresponding coefficients:

$$\boldsymbol{\Phi} := \mathbf{U} = \begin{bmatrix} \boldsymbol{\phi}_1 & \boldsymbol{\phi}_2 & \dots & \boldsymbol{\phi}_r \end{bmatrix}, \ \boldsymbol{\Lambda} := \mathbf{V}\boldsymbol{\Sigma} = \begin{bmatrix} \lambda_1 & \lambda_2 & \dots & \lambda_r \end{bmatrix}. \tag{7}$$

The matrix $\boldsymbol{\Phi}$, composed of columns $\boldsymbol{\phi}_i(t)$, contains the reduced POD basis functions $\{\boldsymbol{\phi}_i(t)\}_{i=1}^{r}$, while $\boldsymbol{\Lambda}$ holds the projection coefficients for the reduced basis. A generic curve $s_k(t)$ belonging to the training dataset, indexed by $k = 1, \dots, n_s$ and evaluated at times $t \in T$, can be approximated in reduced form as:

$$s_k^{(r)}(t) = \sum_{i=1}^{r} \lambda_{k,i}\phi_i(t), \tag{8}$$

and its discrete representation is given by:

$$\mathbf{s}_k^{(r)} = \boldsymbol{\Lambda}_{k,\bullet}\boldsymbol{\Phi}^{\mathrm{T}}, \tag{9}$$

where $\boldsymbol{\Lambda}_{k,\bullet}$ refers to the kth row of the matrix $\boldsymbol{\Lambda}$.

Let us consider now a parametric curve depending on N features $\boldsymbol{p} \in \Omega$, that is $s(t;\boldsymbol{p})$, for $t \in T$. From Eq. (8) it is clear that, once the reduced basis matrix $\boldsymbol{\Phi}$ available, such function is projected over this basis only through the POD (parametric) coefficients $\{\lambda_i(\boldsymbol{p})\}_{i=1}^{r}$:

$$s^{(r)}(t;\boldsymbol{p}) = \sum_{i=1}^{r} \lambda_i(\boldsymbol{p})\phi_i(t). \tag{10}$$

This formulation indicates that a reduced-order parametric metamodel can be built using only the set of coefficients $\lambda_i(\boldsymbol{p})_{i=1}^{r}$. Specifically, the following parametric function can be constructed:

$$\boldsymbol{s}_\lambda(\boldsymbol{p}) = \begin{bmatrix} \lambda_1(\boldsymbol{p}) & \lambda_2(\boldsymbol{p}) & \dots & \lambda_r(\boldsymbol{p}) \end{bmatrix}^{\mathrm{T}} : \Omega \subset \mathbb{R}^d \to \mathbb{R}^r, \tag{11}$$

4.2. Random forest regression

Random Forest is a popular machine learning method that improves prediction accuracy and reduces overfitting by combining multiple decision trees. It is widely applied in regression tasks due to its ability to model nonlinear relationships. As shown in Fig. 7, the Random Forest regression process involves several key steps. First, the input training data is divided into multiple subsets using bootstrap sampling, promoting diversity in the training phase. Each decision tree is then trained on a unique bootstrapped dataset, with random feature selection at each split to minimize tree correlation and enhance generalization. The model comprises multiple independent decision trees, each generating predictions. These predictions are aggregated, typically by averaging, to produce the final output. This workflow, combining bootstrap sampling, random feature selection, and prediction aggregation, underpins the strength and versatility of Random Forest. For further details, refer to [84].

5. Results and discussion

After generating and preprocessing the dataset, which includes input parameters such as the microstructural morphology and fiber orientation of the woven composite laminate, as well as the corresponding macroscopic stress–strain curves, a surrogate model is developed. This model integrates model order reduction with machine learning techniques, as described in the previous section. The combination of these methods led to several key findings which are discussed in the following.

Figs. 8(a) and 8(b) provide an overview of the macroscopic strain–time curves and their corresponding stress–strain responses for 100 randomly selected samples from the entire dataset. The strain–time plot in Fig. 8(a) highlights the variability in strain evolution across different samples, capturing the range of behaviors present in both the training and test data. The overlapping curves showcase the differences in strain response that can arise from varying microstructural geometries and orientations, underscoring the need for accurate modeling and prediction using the Random Forest and POD-based approaches presented in this study.

The stress–strain plot in Fig. 8(b) further illustrates how the stress response varies as a function of strain across these samples. However, for the purpose of model prediction, it is sufficient to focus on the strain–time curves, as these curves directly capture the effects of different microstructural configurations.

5.1. Proper orthogonal decomposition

Fig. 9(a) shows the singular values and the cumulative explained variance for the truncated Proper Orthogonal Decomposition (POD). The singular values (black line) indicate the relative importance of each mode, while the cumulative explained variance (blue dashed line) shows the percentage of total variance captured as a function of the number of retained modes. The shaded gray region highlights the first five modes, which have been retained for further analysis, providing a balance between model complexity and accuracy.

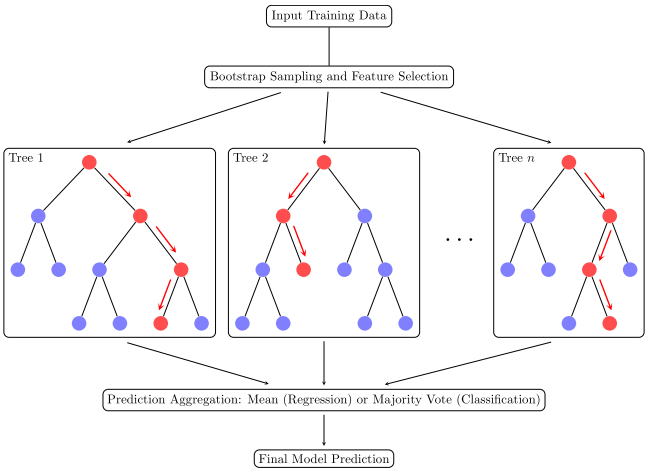

Fig. 7. Schematic of Random Forest Regression: Multiple decision trees are trained on different subsets of the data, and their predictions are averaged to produce the final output.

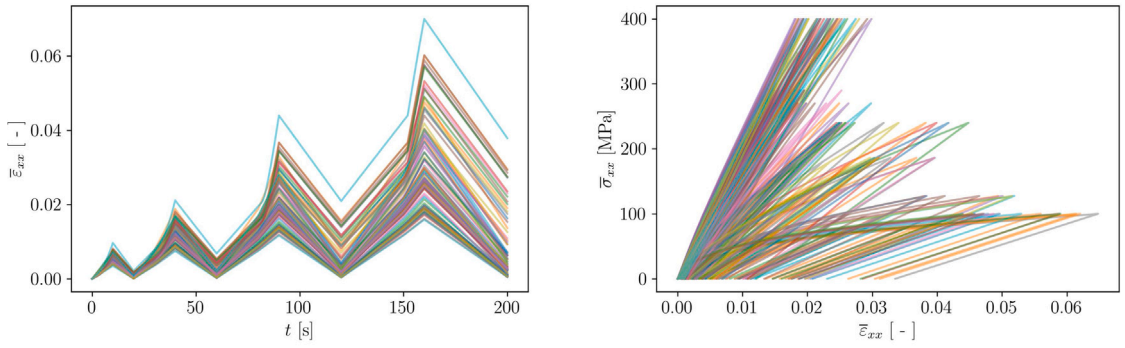

(a) Strain-time curves. (b) Stress-strain curves.

Fig. 8. Overview of the macroscopic strain–time and stress–strain curves from a random selection of 100 samples in the dataset.

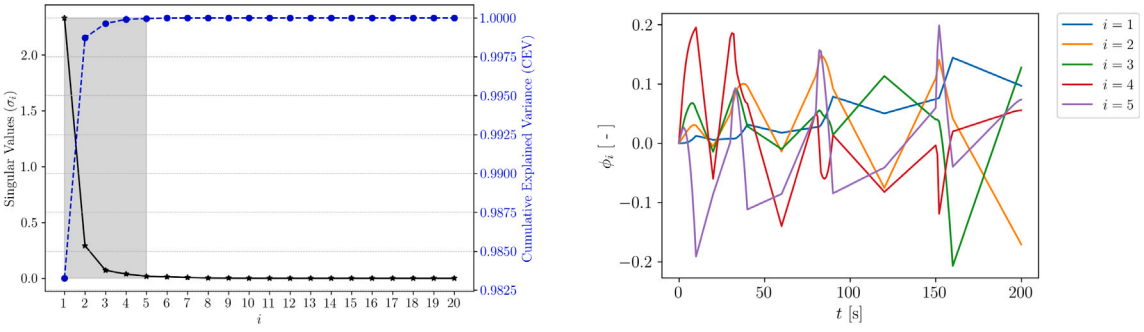

(a) Singular values and cumulative explained variance for the truncated POD.

(b) Temporal evolution of the first 5 POD modes (ϕ_i) as a function of time (t).

Fig. 9. Singular values, cumulative explained variance and modes for the truncated POD.

Fig. 9(b) gives the temporal evolution of the first 5 Proper Orthogonal Decomposition (POD) modes (ϕ_i) as a function of time (t). Each curve represents a distinct mode, illustrating the most significant patterns of variability captured by the POD in the dataset. The legend indicates the mode index (i) for each plotted mode. Fig. 10 illustrates the comparison between the original and POD-reconstructed macroscopic strain–time curves for test datasets, across various microstructural geometries and woven fabric orientations. The close alignment between the original and reconstructed curves for the test dataset indicates that the POD approach has successfully captured the underlying variability and dynamics of the strain response, even for complex microstructures. This high degree of accuracy in the reconstructions demonstrates the effectiveness of the POD-based dimensionality reduction, ensuring that the essential features of the strain–time relationship are preserved while significantly reducing the complexity of the dataset. However, it is important to emphasize that our training process relies on a dataset consisting of four load-unload paths. Consequently, the proposed decomposition is specifically valid for such loading paths. To extend this

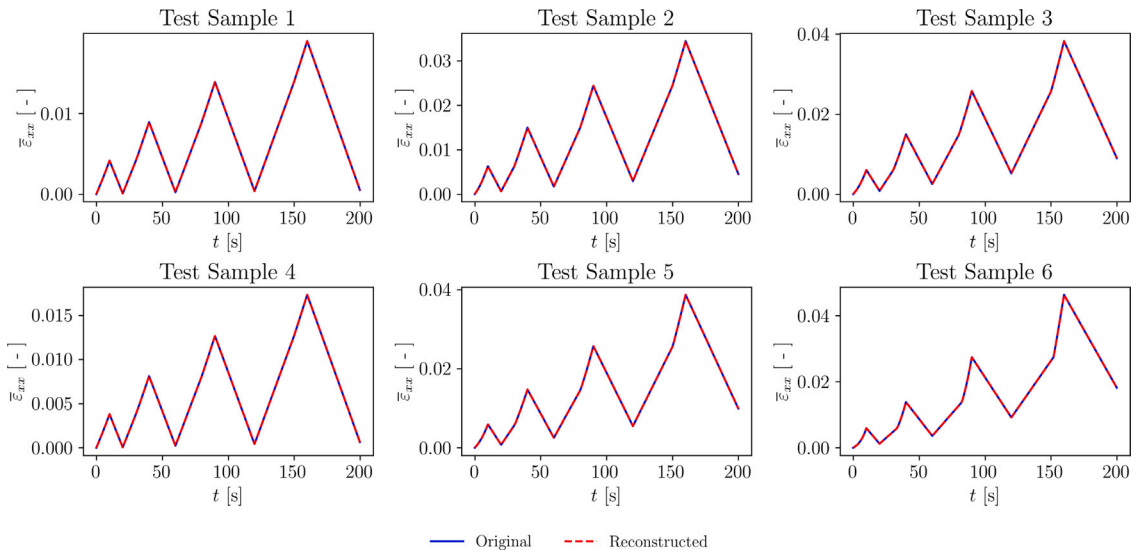

Fig. 10. Comparison of Original vs. POD-Reconstructed macroscopic strain–time curves for the **test** dataset across different microstructural geometries and woven fabric orientations.

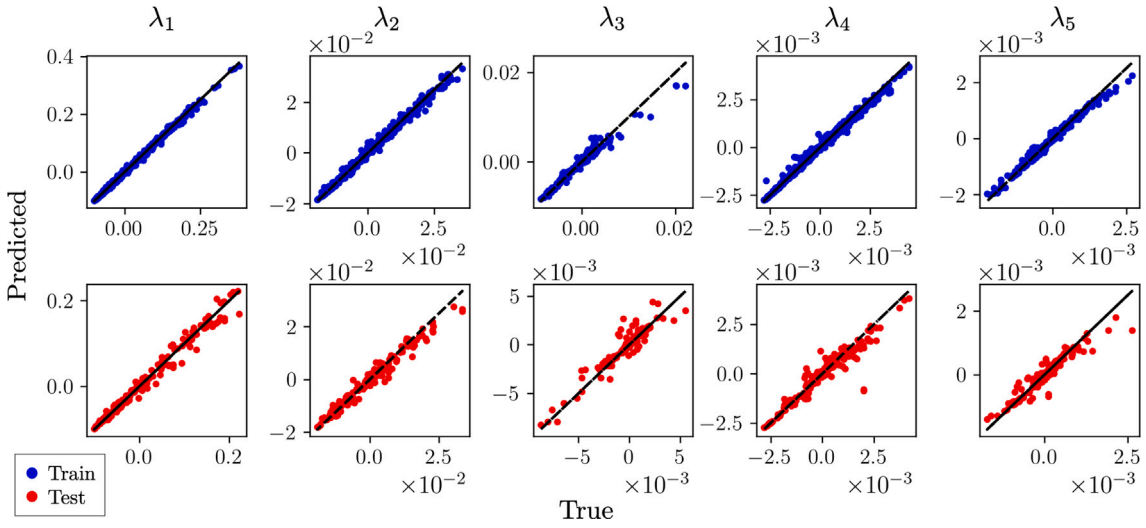

Fig. 11. Comparison of true and Random Forest predicted values for the coefficients λ_1, λ_2, λ_3, λ_4 and λ_5 in both **training** and **test** datasets.

approach to loading paths with varying profiles, techniques such as clustering, classification algorithms, or data alignment strategies could be integrated into the workflow, as suggested in [88].

5.2. Machine learning model

Fig. 11 compares the true values of the coefficients $\lambda_1, \ldots, \lambda_5$ with those predicted by the Random Forest model for both the training and test datasets. The scatter plots illustrate the model's capability to approximate the target values, where points closer to the diagonal line represent better predictive accuracy.

Fig. 12 shows a histogram of the relative L_2 norm errors between the true and predicted values for the test dataset. The relative errors remain consistently below 0.15, demonstrating that the model achieves a good level of accuracy across different test samples. The distribution is left-skewed, indicating that most of the errors are concentrated towards lower values, with only a few instances where the error is relatively higher. This skewness suggests that the model is generally reliable, with occasional challenges in replicating more complex behavior for some samples.

The Fig. 13 illustrates the accuracy of the predictive model by comparing the actual strain–time curves (blue solid lines) against the predicted ones (red dashed lines) for six randomly chosen samples from the test dataset. The close alignment between the actual and predicted curves across varying time intervals indicates that the model is capable of capturing the underlying dynamics of the strain evolution with high precision. These results validate the model's generalization ability and its robustness in reconstructing strain behavior for unseen microstructural configurations.

To further illustrate the performance of the surrogate model, Fig. 14 presents a comparison of the true and predicted stress–strain curves generated by the developed framework. This comparison includes four randomly selected samples from the test dataset, each simulated at three different woven fabric orientations, as detailed in Table 2. The Figure demonstrates a close alignment between the actual and predicted curves across various configurations of composite laminates. These results confirm the model's generalization ability and robustness in accurately reconstructing macroscopic stress–strain curves for unseen configuration of laminates. Although the model demonstrates a high level of accuracy and computational efficiency, further enhancements could be explored through the application of non-intrusive PGD techniques or advanced artificial neural network architectures to improve its performance and generalizability.

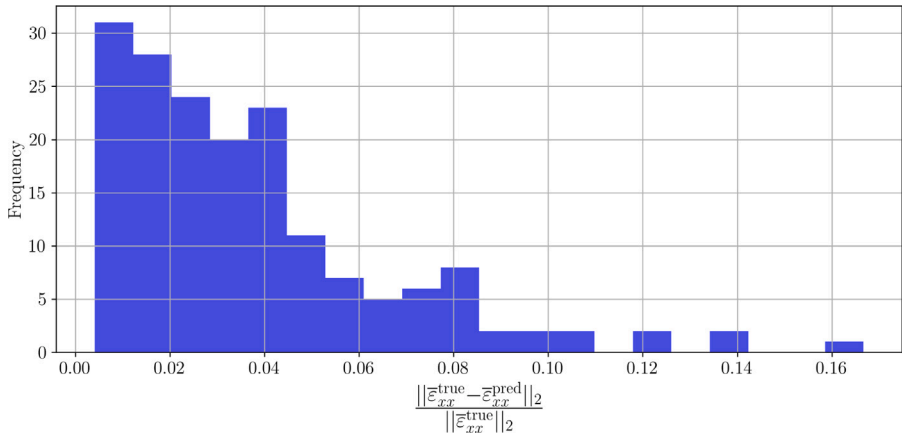

Fig. 12. Histogram of relative L_2 norm errors for the test dataset.

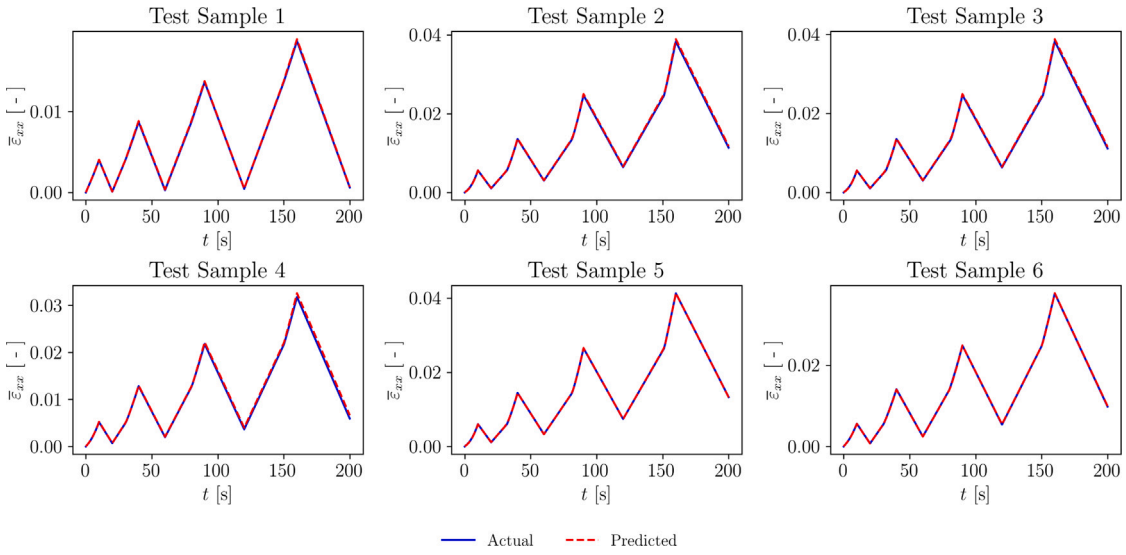

Fig. 13. Comparison of actual vs. predicted macroscopic strain–time curves for randomly selected **test** samples.

Table 2
Microstructural parameter values for four randomly selected microstructures from the **test** dataset of 2/2 twill weave composites, each evaluated at three distinct fabric orientations.

Symbol	Parameter	M_1	M_2	M_3	M_4
p_1	a_1 [mm]	3.223	2.65	1.028	3.803
p_2	a_2 [mm]	3.704	0.8	4.370	1.422
p_3	h [mm]	0.346	0.4	0.264	0.556
p_4	c [mm]	0.393	0.3	0.341	0.395
p_5	θ deg [°]	0.0/30.0/35.0	60.0/67.5/90.0	15.0/50.0/60.0	40.0/45.0/55.0

5.3. Graphical user interface application:

To enable user-friendly interaction with this surrogate model, a Graphical User Interface (GUI) has been developed using MATLAB App Designer, as illustrated in Fig. 15. This application allows designers and engineers to deduce, instantaneously, the macroscopic strain–stress curves of woven composite for any specified set of microstructural parameters. Users can easily modify these parameters through adjustable sliders, accessible via both desktop and mobile applications, thereby eliminating the need for complex microstructure generation and finite element (FE) computations. Such a tool allows hence assessing in real-time the influence of the input parameters on the overall composite behavior. It can be also employed as a decision-making tool towards optimal material selection.

6. Conclusions and perspectives

In this paper, a surrogate model has been developed by combining model order reduction and machine learning techniques to enable real-time virtual testing of symmetric and balanced laminate thermoplastic composites, reinforced with a 2/2 twill weave architecture. The model is specifically designed to capture the inelastic behavior of these composites under load-unload conditions, with a particular emphasis on stiffness degradation due to yarn damage. The key microstructural parameters considered in the model include the width of the weft and warp yarns, fabric thickness, gaps between adjacent yarns, and the woven fabric orientation. The primary advantage of this approach is its ability to eliminate the need for repetitive microstructure generation or finite element simulations when assessing, in nonlinear regime, new laminates: different microstructural parameters

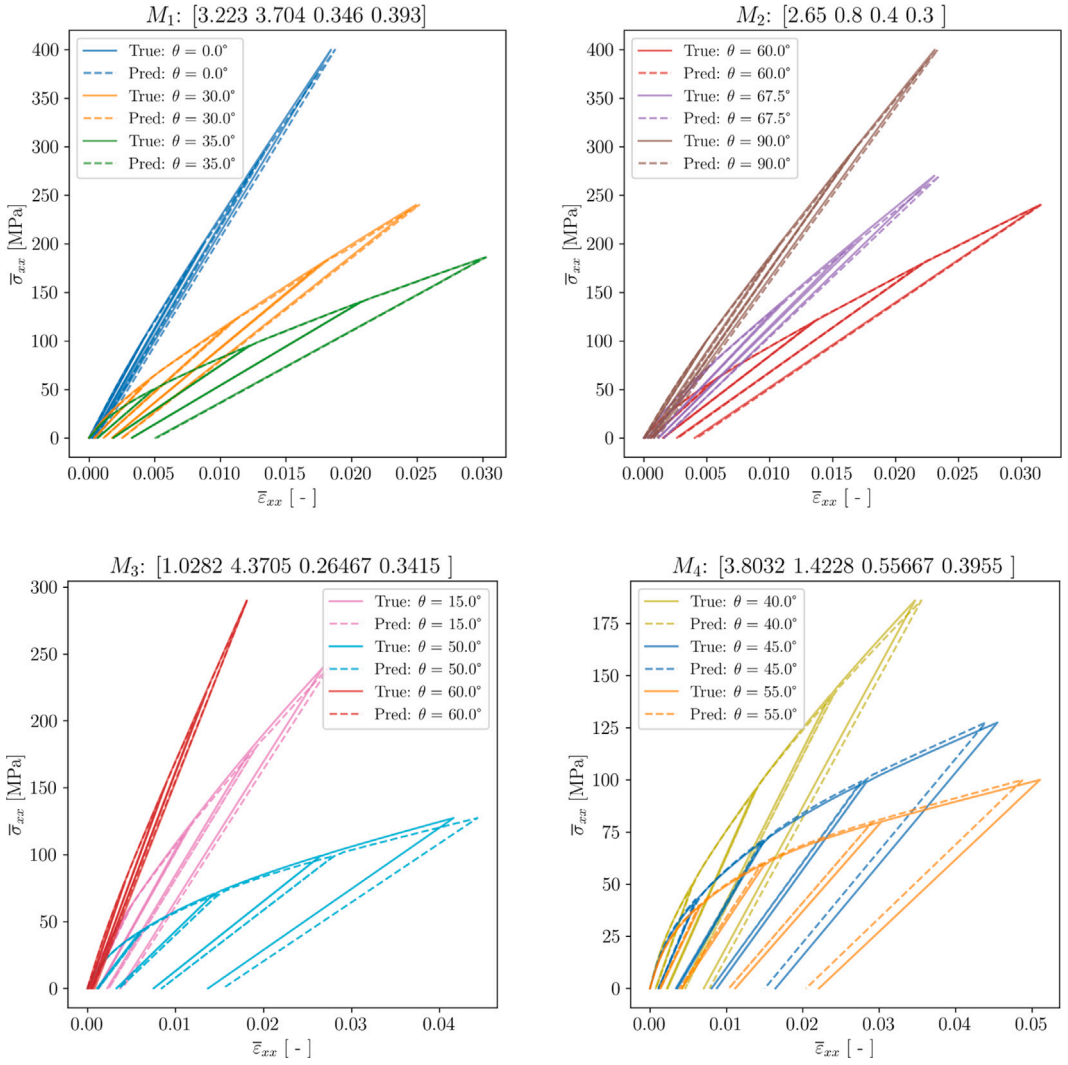

Fig. 14. Comparison of true and predicted stress–strain curves for four randomly selected microstructures (M_1, M_2, M_3 and M_4) from the **test** dataset, each evaluated at three distinct woven fabric orientations.

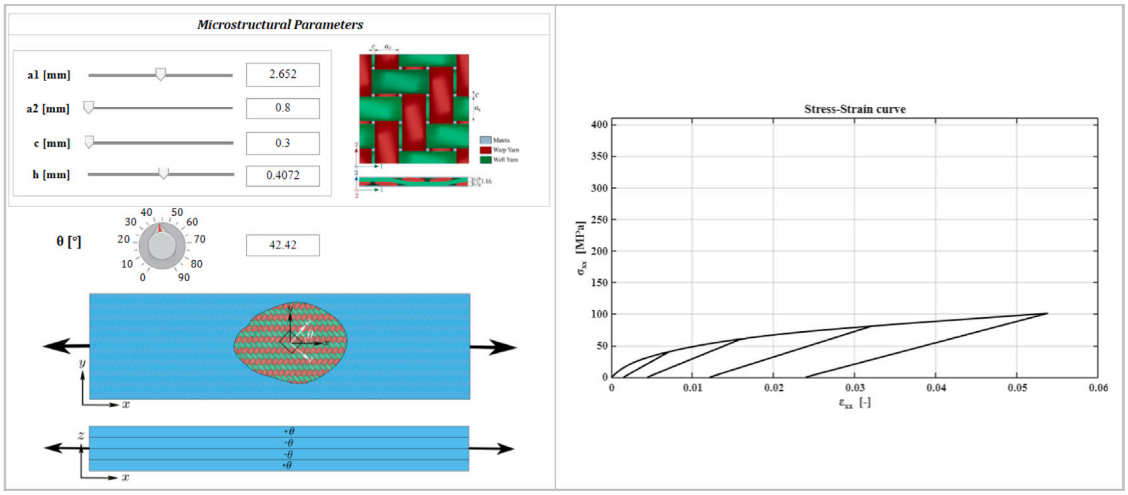

Fig. 15. Graphical User Interface (GUI) application for online prediction of the macroscopic stress–strain curve of laminated composite reinforced with 2/2 twill weave architecture incorporating microstructure parameters (weft width a_1, warp width a_2, yarn spacing c, fabric thickness h) and woven fabric orientation (θ).

and woven fabric plies orientation. This enhances computational efficiency and accelerates the design process of thermoplastic composite materials in various engineering applications. The model's predictive accuracy is validated against stress–strain curves generated from finite element based on periodic homogenization across a wide range of microstructural configurations.

Despite its strengths, this study has certain limitations. The current model parameterizes only the geometry of the 2/2 twill weave and is constrained to a predefined loading path. This means that while it is effective for analyzing loading and unloading conditions under specific stress states, it does not account for alternative loading scenarios, such as cyclic loading or more complex loading paths with varying stress or strain values. These limitations restrict the potential of the model for virtual real-time testing of woven composites, particularly when dealing with diverse and dynamic loading conditions. To overcome these limitations, future work could extend the model by incorporating the loading path as an additional parameter within the surrogate model. This will enable the exploration of more complex interactions between microstructure and different loading conditions.

CRediT authorship contribution statement

M. El Fallaki Idrissi: Writing – original draft, Visualization, Validation, Methodology, Investigation, Formal analysis, Conceptualization. **A. Pasquale:** Writing – original draft, Validation, Methodology, Investigation, Formal analysis. **F. Meraghni:** Writing – review & editing, Supervision, Methodology, Funding acquisition, Formal analysis, Conceptualization. **F. Praud:** Review & editing, Investigation, Formal analysis, Conceptualization. **F. Chinesta:** Writing – review & editing, Supervision, Methodology, Formal analysis, Conceptualization.

Declaration of competing interest

The authors declare the following financial interests/personal relationships which may be considered as potential competing interests: EL FALLAKI IDRISSI Mohammed reports financial support was provided by ESI Group- ENSAM Chair. If there are other authors, they declare that they have no known competing financial interests or personal relationships that could have appeared to influence the work reported in this paper.

Acknowledgments

The authors gratefully acknowledge ESI Chair for the support that greatly assisted this research, and the Arts et Métiers High Performance Computing Center Cassiopee made available for conducting the research reported in this paper.

Appendix. Local constitutive equations of woven composite phases

A.1. Local constitutive model for the matrix

The state laws for the matrix sub-domain, *i.e.*, $\forall \boldsymbol{x} \in \mathfrak{B}_0$, are based on the following form of the Helmholtz free energy density:

$$\Psi(\boldsymbol{\varepsilon}, \boldsymbol{\varepsilon}_p, p) = \frac{1}{2}(\boldsymbol{\varepsilon} - \boldsymbol{\varepsilon}_p) : \mathbb{C}_e : (\boldsymbol{\varepsilon} - \boldsymbol{\varepsilon}_p) + \int_0^p R(\xi)\, \mathrm{d}\xi, \tag{A.1}$$

in which the total strain $\boldsymbol{\varepsilon}$ acts as external state variable, while the plastic strain $\boldsymbol{\varepsilon}_p$ and the equivalent plastic strain p act as internal state variables. Based on thermodynamics considerations [74], it yields for the stress:

$$\boldsymbol{\sigma} = \frac{\partial \Psi}{\partial \boldsymbol{\varepsilon}} = \mathbb{C}_e : (\boldsymbol{\varepsilon} - \boldsymbol{\varepsilon}_p), \tag{A.2}$$

with the following conjugate variables:

$$-\boldsymbol{\sigma} = \frac{\partial \Psi}{\partial \boldsymbol{\varepsilon}_p}, \qquad R = \frac{\partial \Psi}{\partial p} = R(p). \tag{A.3}$$

In the above equations, $\mathbb{C}_e$ stands for fourth order stiffness tensors classically defined for bulk isotropic materials by the Young's modulus E and the Poisson's ratio ν. Additionally, $R(\xi)$ depicts the hardening function, which is expressed as an exponential linear function in the present case:

$$R(p) = Q_1\left(1 - \exp(-bp)\right) + Q_2 p, \tag{A.4}$$

where Q_1, b and Q_2 are hardening parameters.

Following the formalism of associative plasticity, the evolution of the internal state variables p and $\boldsymbol{\varepsilon}_p$ is obtained by the normality rule of the yield function $f(\boldsymbol{\sigma}, R)$, which also activate the plastic multiplier λ through the *Kuhn–Tucker* conditions:

$$f(\boldsymbol{\sigma}, R) = \mathrm{eq}(\boldsymbol{\sigma}) - R(p) - \sigma_y \leq 0 \quad \begin{cases} < 0, & \dot{\lambda} = 0 \\ = 0, & \dot{\lambda} > 0 \end{cases}, \tag{A.5}$$

where $\mathrm{eq}(\boldsymbol{\sigma})$ and σ_y denotes the equivalent von Mises stress and the initial yield threshold. Therefore, it yields for the evolution laws:

$$\dot{p} = -\frac{\partial f}{\partial R}\dot{\lambda} = \dot{\lambda}, \qquad \dot{\boldsymbol{\varepsilon}}_p = \frac{\partial f}{\partial \boldsymbol{\sigma}}\dot{\lambda} = \boldsymbol{\Lambda}(\boldsymbol{\sigma})\dot{p}, \tag{A.6}$$

where $\boldsymbol{\Lambda}(\boldsymbol{\sigma})$ stands for the plastic strain flow, given by:

$$\boldsymbol{\Lambda}(\boldsymbol{\sigma}) = \frac{3}{2}\frac{\mathbf{Dev}(\boldsymbol{\sigma})}{\mathrm{eq}(\boldsymbol{\sigma})}. \tag{A.7}$$

The parameters of the matrix have been identified and the obtained results are listed in Table A.3.

Table A.3
Parameters of the elasto-plastic model identified for PA66 matrix.

Feature	Parameter	Value	Unit
Young's modulus	E	2 074	MPa
Poisson's ratio (standard value)	ν	0.3	–
Yield threshold	σ_y	14	MPa
Hardening parameters	Q_1	30	MPa
	b	160	–
	Q_2	260	MPa

A.2. Local constitutive model for the yarns

For the yarns sub-domains, *i.e.*, $\forall \boldsymbol{x} \in \mathfrak{B}_1 \cup \mathfrak{B}_2$, the state laws derive from the following form of the Helmholtz free energy density:

$$\Psi(\boldsymbol{\varepsilon}, \boldsymbol{\varepsilon}_s, \gamma_c) = \frac{1}{2}(\boldsymbol{\varepsilon} - \boldsymbol{\varepsilon}_s) : \left[\mathbb{C}_0 - \mathbb{D}(\gamma_c)\right] : (\boldsymbol{\varepsilon} - \boldsymbol{\varepsilon}_s), \tag{A.8}$$

where the total strain $\boldsymbol{\varepsilon}$ acts as external state variable. As shown in Fig. 4, a micromechanical description of a RVE containing a micro-cracks density γ_c is utilized to define an anisotropic damage fourth order tensor $\mathbb{D}(\gamma_c)$ that reduces the initially transversely isotropic stiffness tensor $\mathbb{C}_0$. As a result of the micro-cracks non-closure effect, anisotropic damage is often accompanied by apparent permanent deformations [96]. The latter are phenomenologically represented by an inelastic strain tensor, denoted by $\boldsymbol{\varepsilon}_s$. In the present formulation, both γ_c and $\boldsymbol{\varepsilon}_s$ are regarded as internal state variables. Based on thermodynamics considerations, it yields for the stress:

$$\boldsymbol{\sigma} = \frac{\partial \Psi}{\partial \boldsymbol{\varepsilon}} = \left[\mathbb{C}_0 - \mathbb{D}(\gamma_c)\right] : (\boldsymbol{\varepsilon} - \boldsymbol{\varepsilon}_s), \tag{A.9}$$

and for the conjugate variables:

$$-\boldsymbol{\sigma} = \frac{\partial \Psi}{\partial \boldsymbol{\varepsilon}_s}, \qquad -Y_c = \frac{\partial \Psi}{\partial \gamma_c}. \tag{A.10}$$

in the above equations, the damage tensor $\mathbb{D}(\gamma_c)$ is evaluated considering the micromechanical scheme of [97] in which micro-cracks are idealized by quasi-flat ellipsoidal inclusions of void with zero stiffness. Note that the micro-cracks are assumed to have their normal oriented along the second direction $\vec{x}_2$, as depicted in Fig. 4. After proper

calculation, the damage tensor is given by:

$$\mathbb{D}(\gamma_c) = \gamma_c \mathbb{C}_0 : \mathbb{T}_c : \mathbb{A}_0(\gamma_c), \tag{A.11}$$

with

$$\mathbb{T}_c = (\mathbb{I} - \mathbb{S}_E)^{-1}, \qquad \text{and} \qquad \mathbb{A}_0(\gamma_c) = \left(\mathbb{I} + \gamma_c(\mathbb{T}_c - \mathbb{I})\right)^{-1}, \tag{A.12}$$

where $\mathbb{T}_c$ represents the interaction tensor of the void inclusion. The latter is itself defined from the well known Eshelby's tensor $\mathbb{S}_E$ [9], which is numerically assessed [98] from the stiffness tensor of the reference medium, namely $\mathbb{C}_0$, as well as the geometrical configuration of the void inclusion, which is here identical to the one adopted in previous works [52,54,62]. $\mathbb{A}_0(\gamma_c)$ stands for the strain localization tensor which allows to express the strain and stress in the damage free part of the material:

$$\boldsymbol{\varepsilon}_0 = \mathbb{A}_0(\gamma_c) : (\boldsymbol{\varepsilon} - \boldsymbol{\varepsilon}_s), \qquad \boldsymbol{\sigma}_0 = \mathbb{C}_0 : \mathbb{A}_0(\gamma_c) : (\boldsymbol{\varepsilon} - \boldsymbol{\varepsilon}_s). \tag{A.13}$$

To drive the damage evolution, an Hill-like damage activation criterion [99] is defined from the stress in the damage free part of the material:

$$H_c(\boldsymbol{\sigma}_0) = \sqrt{\boldsymbol{\sigma}_0 : \mathbb{H} : \boldsymbol{\sigma}_0} = \sqrt{\left(\frac{\sigma_{0_{22}}}{R_{22}}\right)^2 + \left(\frac{\sigma_{0_{12}}}{R_{12}}\right)^2}, \tag{A.14}$$

where $\mathbb{H}$ is a fourth-order tensor involving the initial damage thresholds in pure transverse tension R_{22} and in pure in-plane shear R_{12} in such a way that the damage multiplier λ is only activated under those loading modes through the following Kuhn–Tucker conditions:

$$g(H_c) - \gamma_c \leq 0 \quad \begin{cases} < 0, & \dot{\lambda} = 0 \\ = 0, & \dot{\lambda} > 0 \end{cases}. \tag{A.15}$$

In this relationship, $g(H_c)$ denotes a damage development function chosen as a Weibull-like function [100] in the present formulation:

$$g(H_c) = \gamma_c^{\infty}\left[1 - \exp\left(-\left[\frac{\langle H_c - 1\rangle_+}{S}\right]^{\beta}\right)\right], \tag{A.16}$$

where S, β and γ_c^{∞} are material parameters.

The evolution laws assume that damage growth and the development of inelastic strains are coupled and simultaneously activated. Such evolution is formulated in the context of a non-associative deformation mechanism through the normality rule of an indicative function given by:

$$F(\boldsymbol{\sigma}, Y_c) = H_s(\boldsymbol{\sigma}) + Y_c, \tag{A.17}$$

where $H_s(\boldsymbol{\sigma})$ represents a quadratic interaction surface:

$$H_s(\boldsymbol{\sigma}) = \sqrt{\boldsymbol{\sigma} : \mathbb{F} : \boldsymbol{\sigma}} = \sqrt{(a_{22}\sigma_{22})^2 + (a_{12}\sigma_{12})^2}, \tag{A.18}$$

in which, the fourth order tensor $\mathbb{F}$ involves the inelasticity parameters in transverse tension and in-plane shear inelasticity, a_{22} and a_{12}, respectively. Therefore, it results the following evolution laws:

$$\dot{\gamma}_c = \frac{\partial F}{\partial Y_c}\dot{\lambda} = \dot{\lambda}, \qquad \dot{\boldsymbol{\varepsilon}}_s = \frac{\partial F}{\partial \boldsymbol{\sigma}}\dot{\lambda} = \boldsymbol{\Lambda}_s(\boldsymbol{\sigma})\dot{\gamma}_c \tag{A.19}$$

where $\boldsymbol{\Lambda}_s(\boldsymbol{\sigma})$ stands for the inelastic strain flow:

$$\boldsymbol{\Lambda}_s(\boldsymbol{\sigma}) = \frac{\mathbb{F} : \boldsymbol{\sigma}}{H_s(\boldsymbol{\sigma})}. \tag{A.20}$$

that only has its 22 and 12 components active, due to the form of $H_s(\boldsymbol{\sigma})$ in Eq. (A.18).

The yarns parameters are then identified from the macroscopic response of the entire woven composite through reverse techniques on the reference microstructure and the obtained values are listed in Table A.4.

Table A.4
Parameters of the constitutive model of the yarns identified from the macroscopic response of the whole woven composite for the reference microstructure.

Feature	Parameter	Value	Unit
Transversely isotropic stiffness tensor	$C_{0_{1111}}$	65 822	MPa
(non-null components)	$C_{0_{1122}} = C_{0_{1133}}$	7 041	MPa
	$C_{0_{2222}} = C_{0_{3333}}$	23 947	MPa
	$C_{0_{2233}}$	6 971	MPa
	$C_{0_{1212}} = C_{0_{1313}}$	8 661	MPa
	$C_{0_{2323}} = \frac{1}{2}(C_{0_{2222}} - C_{0_{2233}})$	8 488	MPa
Pure transverse tension threshold	R_{22}	20.0	MPa
Pure in-plane shear threshold	R_{12}	4.5	MPa
Weibull parameters	S	12.3	–
	β	2.75	–
	γ_c^{∞}	0.025	–
Transverse tension inelasticity parameter	a_{22}	1.5	–
In-plane shear inelasticity parameter	a_{12}	1.0	–

Data availability

Data will be made available on request.

References

[1] M. Bhong, T.K. Khan, K. Devade, B.V. Krishna, S. Sura, H. Eftikhaar, H.P. Thethi, N. Gupta, Review of composite materials and applications, Mater. Today: Proc. (2023).

[2] A. Wazeer, A. Das, C. Abeykoon, A. Sinha, A. Karmakar, Composites for electric vehicles and automotive sector: A review, Green Energy Intell. Transp. 2 (1) (2023) 100043.

[3] A.E. Krauklis, C.W. Karl, A.I. Gagani, J.K. Jørgensen, Composite material recycling technology—state-of-the-art and sustainable development for the 2020s, J. Compos. Sci. 5 (1) (2021) 28.

[4] M. Nachtane, F. Meraghni, G. Chatzigeorgiou, L. Harper, F. Pelascini, Multiscale viscoplastic modeling of recycled glass fiber-reinforced thermoplastic composites: Experimental and numerical investigations, Composites B 242 (2022) 110087.

[5] S.E. Sekkal, F. Meraghni, G. Chatzigeorgiou, L. Peltier, N. Durand, Experimental and multiscale investigation of the mechanical behavior of mechanically recycled glass fiber reinforced thermoplastic composites, Composites B (2023) 110925.

[6] A.C. Long, Design and manufacture of textile composites, CRC Press, 2006.

[7] D. Gay, S.V. Hoa, Composite materials: design and applications, CRC Press, 2007.

[8] G. Chatzigeorgiou, F. Meraghni, N. Charalambakis, Multiscale Modeling Approaches for Composites, Elsevier, 2022.

[9] J.D. Eshelby, The determination of the elastic field of an ellipsoidal inclusion, and related problems, Proc. R. Soc. Lond. Ser. A. Math. Phys. Sci. 241 (1226) (1957) 376–396.

[10] M. Barral, G. Chatzigeorgiou, F. Meraghni, R. Léon, Homogenization using modified mori-tanaka and TFA framework for elastoplastic-viscoelastic-viscoplastic composites: Theory and numerical validation, Int. J. Plast. 127 (2020) 102632.

[11] Q. Chen, G. Chatzigeorgiou, F. Meraghni, Extended mean-field homogenization of viscoelastic-viscoplastic polymer composites undergoing hybrid progressive degradation induced by interface debonding and matrix ductile damage, Int. J. Solids Struct. 210 (2021) 1–17.

[12] Q. Chen, G. Chatzigeorgiou, G. Robert, F. Meraghni, Combination of mean-field micromechanics and cycle jump technique for cyclic response of PA66/GF composites with viscoelastic–viscoplastic and damage mechanisms, Acta Mech. (2023) 1–20.

[13] M. Kamiński, Boundary element method homogenization of the periodic linear elastic fiber composites, Eng. Anal. Bound. Elem. 23 (10) (1999) 815–823.

[14] G. Chatzigeorgiou, N. Charalambakis, Y. Chemisky, F. Meraghni, Periodic homogenization for fully coupled thermomechanical modeling of dissipative generalized standard materials, Int. J. Plast. 81 (2016) 18–39.

[15] Q. Chen, F. Meraghni, G. Chatzigeorgiou, Recursive multiscale homogenization of multiphysics behavior of fuzzy fiber composites reinforced by hollow carbon nanotubes, J. Intell. Mater. Syst. Struct. (2022) 1045389X221111545.

[16] H. Moulinec, P. Suquet, A numerical method for computing the overall response of nonlinear composites with complex microstructure, Comput. Methods Appl. Mech. Engrg. 157 (1–2) (1998) 69–94.

[17] M. Schneider, A review of nonlinear FFT-based computational homogenization methods, Acta Mech. 232 (6) (2021) 2051–2100.

[18] F. Praud, K. Schneider, G. Chatzigeorgiou, F. Meraghni, Microstructure generation and full-field multiscale analyses for short fiber reinforced thermoplastics: Application to PA66gf composites, Compos. Struct. 341 (2024) 118175.

[19] M.F. Arif, F. Meraghni, Y. Chemisky, N. Despringre, G. Robert, In situ damage mechanisms investigation of PA66/GF30 composite: Effect of relative humidity, Composites B 58 (2014) 487–495.

[20] A. Malpot, F. Touchard, S. Bergamo, Effect of relative humidity on mechanical properties of a woven thermoplastic composite for automotive application, Polym. Test. 48 (2015) 160–168.

[21] R. Chekkour, A. Benaarbia, G. Chatzigeorgiou, F. Meraghni, G. Robert, Effect of thermo-hygro glycol aging on the damage mechanisms of short glass-fiber reinforced polyamide 66, Composites A 165 (2023) 107358.

[22] S. Satouri, R. Chekkour, G. Chatzigeorgiou, F. Meraghni, G. Robert, Numerical-experimental approach to identify the effect of relative humidity on the material parameters of a rate-dependent damage model for polyamide 66, Mech. Mater. 184 (2023) 104735.

[23] M. Nachtane, M. El Fallaki Idrissi, M. Tarfaoui, Y. Qarssis, A. Abichou, A. Faik, Deep learning-driven predictive tools for damage prediction and optimization in composite hydrogen storage tanks, Compos. Commun. (2024) 102079.

[24] M. Zhang, H. Lv, H. Kang, W. Zhou, C. Zhang, A literature review of failure prediction and analysis methods for composite high-pressure hydrogen storage tanks, Int. J. Hydrog. Energy 44 (47) (2019) 25777–25799.

[25] A. El Moumen, T. Kanit, A. Imad, H. El Minor, Effect of reinforcement shape on physical properties and representative volume element of particles-reinforced composites: statistical and numerical approaches, Mech. Mater. 83 (2015) 1–16.

[26] O. Erol, B.M. Powers, M. Keefe, Effects of weave architecture and mesoscale material properties on the macroscale mechanical response of advanced woven fabrics, Composites A 101 (2017) 554–566.

[27] F. Chinesta, A. Leygue, F. Bordeu, J.V. Aguado, E. Cueto, D. González, I. Alfaro, A. Ammar, A. Huerta, PGD-based computational vademecum for efficient design, optimization and control, Arch. Comput. Methods Eng. 20 (2013) 31–59.

[28] J. Wei, X. Chu, X.-Y. Sun, K. Xu, H.-X. Deng, J. Chen, Z. Wei, M. Lei, Machine learning in materials science, InfoMat 1 (3) (2019) 338–358.

[29] A. Ammar, A. Huerta, F. Chinesta, E. Cueto, A. Leygue, Parametric solutions involving geometry: a step towards efficient shape optimization, Comput. Methods Appl. Mech. Engrg. 268 (2014) 178–193.

[30] F. Chinesta, E. Cueto, E. Abisset-Chavanne, J.L. Duval, F.E. Khaldi, Virtual, digital and hybrid twins: a new paradigm in data-based engineering and engineered data, Arch. Comput. Methods Eng. 27 (1) (2020) 105–134.

[31] A. Leon, S. Mueller, P. de Luca, R. Said, J.-L. Duval, F. Chinesta, Non-intrusive proper generalized decomposition involving space and parameters: application to the mechanical modeling of 3D woven fabrics, Adv. Model. Simul. Eng. Sci. 6 (1) (2019) 1–20.

[32] M. El Fallaki Idrissi, F. Praud, V. Champaney, F. Chinesta, F. Meraghni, Multiparametric modelling of composite materials based on non-intrusive PGD informed by multiscale analyses: Application for real-time stiffness prediction of woven composites, Elsevier, 2022.

[33] Y. Lu, N. Blal, A. Gravouil, Adaptive sparse grid based HOPGD: Toward a nonintrusive strategy for constructing space-time welding computational vademecum, Internat. J. Numer. Methods Engrg. 114 (13) (2018) 1438–1461.

[34] A. Pasquale, V. Champaney, Y. Kim, N. Hascoët, A. Ammar, F. Chinesta, A parametric metamodel of the vehicle frontal structure accounting for material properties and strain-rate effect: application to full frontal rigid barrier crash test, Heliyon 8 (12) (2022).

[35] A. Sancarlos, C. Ghnatios, J.-L. Duval, N. Zerbib, E. Cueto, F. Chinesta, Fast computation of multiparametric electromagnetic fields in synchronous machines by using pgd-based fully separated representations, Energies 14 (5) (2021) 1454.

[36] A. Schmid, A. Pasquale, C. Ellersdorfer, V. Champaney, M. Raffler, S. Guévelou, S. Kizio, M. Ziane, F. Feist, F. Chinesta, PGD based meta modelling of a lithium-ion battery for real time prediction, Front. Mater. 10 (2023) 1245347.

[37] X. Qing, Y. Liao, Y. Wang, B. Chen, F. Zhang, Y. Wang, Machine learning based quantitative damage monitoring of composite structure, Int. J. Smart Nano Mater. 13 (2) (2022) 167–202.

[38] C.E. Okafor, S. Iweriolor, O.I. Ani, S. Ahmad, S. Mehfuz, G.O. Ekwueme, O.E. Chukwumuanya, S.E. Abonyi, I.E. Ekengwu, O.P. Chikelu, Advances in machine learning-aided design of reinforced polymer composite and hybrid material systems, Hybrid Adv. 2 (2023) 100026.

[39] J. Loh, K. Yeoh, K. Raju, V. Pham, V. Tan, T. Tay, A review of machine learning for progressive damage modelling of fiber-reinforced composites, Appl. Compos. Mater. (2024) 1–38.

[40] X. Liu, S. Tian, F. Tao, W. Yu, A review of artificial neural networks in the constitutive modeling of composite materials, Composites B 224 (2021) 109152.

[41] F. Ghavamian, A. Simone, Accelerating multiscale finite element simulations of history-dependent materials using a recurrent neural network, Comput. Methods Appl. Mech. Engrg. 357 (2019) 112594.

[42] L. Wu, N.G. Kilingar, L. Noels, et al., A recurrent neural network-accelerated multiscale model for elasto-plastic heterogeneous materials subjected to random cyclic and non-proportional loading paths, Comput. Methods Appl. Mech. Engrg. 369 (2020) 113234.

[43] S. Gajek, M. Schneider, T. Böhlke, On the micromechanics of deep material networks, J. Mech. Phys. Solids 142 (2020) 103984.

[44] A. Danoun, E. Prulière, Y. Chemisky, FE-LSTM: A hybrid approach to accelerate multiscale simulations of architectured materials using recurrent neural networks and finite element analysis, Comput. Methods Appl. Mech. Engrg. 429 (2024) 117192.

[45] E. Ghane, M. Fagerström, M. Mirkhalaf, Recurrent neural networks and transfer learning for predicting elasto-plasticity in woven composites, Eur. J. Mech. A Solids 107 (2024) 105378.

[46] M. El Fallaki Idrissi, F. Praud, F. Meraghni, F. Chinesta, G. Chatzigeorgiou, Multiscale thermodynamics-informed neural networks (MuTINN) towards fast and frugal inelastic computation of woven composite structures, J. Mech. Phys. Solids 186 (2024) 105604.

[47] F. Masi, I. Stefanou, Multiscale modeling of inelastic materials with thermodynamics-based artificial neural networks (TANN), Comput. Methods Appl. Mech. Engrg. 398 (2022) 115190.

[48] E. Ghane, M. Fagerström, S. Mirkhalaf, A multiscale deep learning model for elastic properties of woven composites, Int. J. Solids Struct. 282 (2023) 112452.

[49] J. Wang, S. Karimi, P. Zeinalzad, J. Zhang, Z. Gong, Using machine learning and experimental study to correlate and predict accelerated aging with natural aging of GFRP composites in hygrothermal conditions, Constr. Build. Mater. 438 (2024) 137264.

[50] H. Liang, W. Li, Y. Li, Y. Li, Machine learning-based multi-objective optimization and physical-geometrical competitive mechanisms for 3D woven thermal protection composites, Int. J. Heat Mass Transfer 232 (2024) 125920.

[51] M. El Fallaki Idrissi, F. Praud, F. Chinesta, F. Meraghni, PGD non-intrusive pour la simulation multiparamétrique en temps réel du comportement non-linéaire des composites à renforts tissés intégrant les paramètres microstructuraux, in: JournÉEs Nationales sur Les Composites 2023, Association pour les MAtériaux Composites (AMAC), 2023, p. 8p.

[52] F. Praud, G. Chatzigeorgiou, Y. Chemisky, F. Meraghni, Hybrid micromechanical-phenomenological modelling of anisotropic damage and anelasticity induced by micro-cracks in unidirectional composites, Compos. Struct. 182 (2017) 223–236.

[53] F. Praud, G. Chatzigeorgiou, J. Bikard, F. Meraghni, Phenomenological multi-mechanisms constitutive modelling for thermoplastic polymers, implicit implementation and experimental validation, Mech. Mater. 114 (2017) 9–29.

[54] F. Praud, G. Chatzigeorgiou, F. Meraghni, Fully integrated multiscale modelling of damage and time-dependency in thermoplastic-based woven composites, Int. J. Damage Mech. 30 (2) (2021) 163–195.

[55] E. Tikarrouchine, G. Chatzigeorgiou, Y. Chemisky, F. Meraghni, Fully coupled thermo-viscoplastic analysis of composite structures by means of multiscale three-dimensional finite element computations, Int. J. Solids Struct. 164 (2019) 120–140.

[56] E. Tikarrouchine, A. Benaarbia, G. Chatzigeorgiou, F. Meraghni, Non-linear FE2 multiscale simulation of damage, micro and macroscopic strains in polyamide 66-woven composite structures: analysis and experimental validation, Compos. Struct. 255 (2021) 112926.

[57] N. Lange, G. Hütter, B. Kiefer, An efficient monolithic solution scheme for FE2 problems, Comput. Methods Appl. Mech. Engrg. 382 (2021) 113886.

[58] C. Hochard, P.A. Aubourg, J.P. Charles, Modelling of the mechanical behaviour of woven-fabric CFRP laminates up to failure, Compos. Sci. Technol. 61 (2001) 221–230.

[59] Y. Thollon, C. Hochard, A general damage model for woven fabric composite laminates up to first failure, Mech. Mater. 41 (7) (2009) 820–827.

[60] C. Hochard, Y. Thollon, A generalized damage model for woven ply laminates under static and fatigue loading conditions, Int. J. Fatigue 32 (2010) 158–165.

[61] N. Feld, F. Coussa, B. Delattre, A novel approach for the strain rate dependent modelling of woven composites, Compos. Struct. 192 (2018) 568–576.

[62] F. Praud, Multiscale modelling of thermoplastic-based woven composites, cyclic and time-dependent behaviour (Ph.D. thesis), Arts et Métiers ParisTech, 2018.

[63] H. Lin, L.-P. Brown, A.-C. Long, Modelling and simulating textile structures using TexGen, Adv. Mater. Res. 331 (2011) 44–47.

[64] L.P. Brown, A.C. Long, Modelling the geometry of textile reinforcements for composites: TexGen, in: P. Boisse (Ed.), Composite Reinforcements for Optimum Performance, Second Edi, Elsevier, 2020.

[65] R. Hill, The essential structure of constitutive laws for metal composites and polycrystals, J. Mater. Sci. Eng. 15 (2) (1967) 79–95.

[66] T. Mura, Micromechanics of defects in solids, second ed., Martinus Nijhoff publishers, 1987.

[67] S. Nemat-Nasser, M. Hori, Micromechanics: Overall Properties of Heterogeneous Materials, second ed., North Holland, 1999.

[68] P. Suquet, Elements of homogenization for inelastic solid mechanics, Lecture Notes in Phys. 272 (1987) 193–278.

[69] J.-C. Michel, H. Moulinec, P. Suquet, Effective properties of composite materials with periodic microstructure: a computational approach, Comput. Methods Appl. Mech. Engrg. 172 (1999) 109–143.

[70] S. Li, On the unit cell for micromechanical analysis of fibre-reinforced composites, Proc. R. Soc. Lond. A 455 (1983) (1999) 815–838.

[71] S. Li, General unit cells for micromechanical analyses of unidirectional composites, Composites A 32 (2001) 815–826.

[72] S. Li, A. Wongsto, Unit cells for micromechanical analyses of particle-reinforced composites, Mech. Mater. 36 (2004) 543–572.

[73] J.L. Chaboche, Constitutive equations for plasticity and viscoplasticity, Int. J. Plast. 5 (1989) 247–302.

[74] J. Lemaitre, J.-L. Chaboche, Mechanics of solid materials, Cambridge University Press, 1994.
[75] J.L. Chaboche, A review of some plasticity and viscoplasticity constitutive theories, Int. J. Plast. 24 (2008) 1642–1693.
[76] F. Meraghni, H. Nouri, N. Bourgeois, C. Czarnota, P. Lory, Parameters identification of fatigue damage model for short glass fiber reinforced polyamide (PA6-GF30) using digital image correlation, Procedia Eng. 10 (2011) 2110–2116.
[77] F. Meraghni, Y. Chemisky, B. Piotrowski, R. Echchorfi, N. Bourgeois, E. Patoor, Parameter identification of a thermodynamic model for superelastic shape memory alloys using analytical calculation of the sensitivity matrix, Eur. J. Mech. A Solids 45 (2014) 226–237.
[78] P. Benner, M. Ohlberger, A. Cohen, K. Willcox, in: P. Benner, M. Ohlberger, A. Cohen, K. Willcox (Eds.), Model Reduction and Approximation, Society for Industrial and Applied Mathematics, Philadelphia, PA, 2017.
[79] G. Rozza, M. Hess, G. Stabile, M. Tezzele, F. Ballarin, C. Gräß le, M. Hinze, S. Volkwein, F. Chinesta, P. Ladeveze, Y. Maday, A. Patera, C. Farhat, S. Grimberg, A. Manzoni, A. Quarteroni, A. Buhr, L. Iapichino, J. Kutz, Model Order Reduction: Volume 3: Applications, De Gruyter, 2020.
[80] G. Rozza, M. Hess, G. Stabile, M. Tezzele, F. Ballarin, C. Gräß le, M. Hinze, S. Volkwein, F. Chinesta, P. Ladeveze, Y. Maday, A. Patera, C. Farhat, S. Grimberg, A. Manzoni, A. Quarteroni, A. Buhr, L. Iapichino, J. Kutz, Volume 2 snapshot-based methods and algorithms, De Gruyter, 2020.
[81] T. Hastie, R. Tibshirani, J. Friedman, New York, NY, USA.
[82] A. Smola, B. Schölkopf, A tutorial on support vector regression, Stat. Comput. 14 (3) (2004) 199–222.
[83] L. Breiman, Classification and regression trees, Routledge, 2017.
[84] L. Breiman, Random forests, Mach. Learn. 45 (2001) 5–32.
[85] R. Ibáñez Pinillo, E. Abisset-Chavanne, A. Ammar, D. González, E. Cueto, A. Huerta, J. Duval, F. Chinesta, A multidimensional data-driven sparse identification technique: The sparse proper generalized decomposition, Complexity 2018 (2018) 1–11.
[86] A. Sancarlos, V. Champaney, E. Cueto, F. Chinesta, Regularized regressions for parametric models based on separated representations, Adv. Model. Simul. Eng. Sci. 10 (2023).
[87] V. Champaney, F. Chinesta, E. Cueto, Engineering empowered by physics-based and data-driven hybrid models: A methodological overview, Int. J. Mater. Form. 15 (2022).
[88] V. Champaney, A. Pasquale, A. Ammar, F. Chinesta, Parametric curves metamodelling based on data clustering, data alignment, POD-based modes extraction and PGD-based nonlinear regressions, Front. Mater. 9 (2022) 904707.
[89] A. Pasquale, V. Champaney, Y. Kim, N. Hascoët, A. Ammar, F. Chinesta, A parametric metamodel of the vehicle frontal structure accounting for material properties and strain-rate effect: application to full frontal rigid barrier crash test, Heliyon 8 (2022) e12397.
[90] A. Schmid, A. Pasquale, C. Ellersdorfer, V. Champaney, M. Raffler, S. Guévelou, S. Kizio, M. Ziane, F. Feist, F. Chinesta, PGD based meta modelling of a lithium-ion battery for real time prediction, Front. Mater. (Comput. Mater. Science) 10 (2023).
[91] A. Schmid, A. Pasquale, C. Ellersdorfer, M. Raffler, V. Champaney, M. Ziane, F. Chinesta, F. Feist, Mechanical characterization of li-ion cells and the calibration of numerical models using proper generalized decomposition, in: Proceedings of the ASME 2023 International Mechanical Engineering Congress and Exposition IMECE2023, 2023.
[92] S. Rodriguez, E. Monteiro, N. Mechbal, M. Rébillat, F. Chinesta, Hybrid twin of RTM process at the scarce data limit, Int. J. Mater. Form. 16 (2023).
[93] R. Zimmermann, Manifold interpolation and model reduction, 2019, arXiv preprint arXiv:1902.06502.
[94] O. Friderikos, E. Baranger, M. Olive, D. Néron, On the stability of POD basis interpolation on grassmann manifolds for parametric model order reduction, Comput. Mech. 70 (1) (2022) 181–204.
[95] I. Goodfellow, Y. Bengio, A. Courville, Deep Learning, MIT Press.
[96] P. Marguères, F. Meraghni, Damage induced anisotropy and stiffness reduction evaluation in composite materials using ultrasonic wave transmission, Composites A 45 (2013) 134–144.
[97] T. Mori, K. Tanaka, Average stress in matrix and average elastic energy of materials with misfitting inclusions, Acta Metall. 21 (1973) 571–574.
[98] A.-C. Gavazzi, D.-C. Lagoudas, On the numerical evaluation of eshelby's tensor and its application to elastoplastic fibrous composites, Comput. Mech. 7 (1990) 13–19.
[99] R. Hill, A theory of the yielding and plastic flow of anisotropic metals, Proc. R. Soc. Lond. A 193 (1033) (1948) 281–297.
[100] W. Weibull, A statistical distribution function of wide applicability, J. Appl. Mech. 18 (1951) 293–297.